nature materials

ARTICLES

https://doi.org/10.1038/s41563-020-0732-6

Check for updates

Configurable phonon polaritons in twisted α-MoO_3

Mingyuan Chen[1,4], Xiao Lin[2,4], Thao H. Dinh[3], Zhiren Zheng[3], Jialiang Shen[1], Qiong Ma[3], Hongsheng Chen[2], Pablo Jarillo-Herrero[3] and Siyuan Dai[1]✉

Moiré engineering is being intensively investigated as a method to tune the electronic, magnetic and optical properties of twisted van der Waals materials. Advances in moiré engineering stem from the formation of peculiar moiré superlattices at small, specific twist angles. Here we report configurable nanoscale light-matter waves—phonon polaritons—by twisting stacked α-phase molybdenum trioxide (α-MoO_3) slabs over a broad range of twist angles from 0° to 90°. Our combined experimental and theoretical results reveal a variety of polariton wavefront geometries and topological transitions as a function of the twist angle. In contrast to the origin of the modified electronic band structure in moiré superlattices, the polariton twisting configuration is attributed to the electromagnetic interaction of highly anisotropic hyperbolic polaritons in stacked α-MoO_3 slabs. These results indicate twisted α-MoO_3 to be a promising platform for nanophotonic devices with tunable functionalities.

Van der Waals (vdW) structures offer a platform to design quantum materials via twisting and stacking of weakly bonded atomic layers[1,2]. This configuration has been recently investigated for the special case of moiré superlattices—the interference lattice pattern obtained by twisting stacked vdW materials at small twist angles δ—which can be used to tune the electronic, magnetic, optical and mechanical properties of the heterostructures. Important results were first reported in electronics[3–6], where moiré superlattices led to the observation of Hofstadter's butterfly, superconductivity, correlated insulating states and other exotic phases of matter. Subsequently, ferromagnetism[7] and moiré excitons[8–11] were reported in vdW structures at small magic twisting angles. In nanophotonics and polaritonic nano-optics, research into which involves highly confined light–matter waves called polaritons[12,13], moiré superlattices were shown to reflect plasmon polaritons in graphene[14–17] and produce nanolight photonic crystals[15].

These previous breakthroughs in configuring vdW materials rely on peculiarities in the formed moiré superlattice as a special case of vdW configuration at small, specific twisting angles (typically $\delta < 5°$). To further exploit the advances of vdW systems, we believe it is worth exploring the configuration of their physical properties via stacking and twisting beyond this δ range. However, polaritons in vdW systems without evident moiré superlattices remain rigid for a broad range of twisting angles ($\delta > 5°$). This lack of configurability stems from the spreading nature of polaritons in most vdW materials: once excited, the polaritons propagate in all directions in the basal plane. The insufficient electromagnetic anisotropy of the spreading propagation weakens the twisting tunability of polaritons based on the rotation of components of the vdW system.

Here we report configurable phonon polaritons—light coupled to lattice vibrations—in twisted α-phase molybdenum trioxide (α-MoO_3) slabs. Unlike other spreading polaritons, phonon polaritons in α-MoO_3 (refs. [18,19]) are extremely anisotropic: they propagate only along certain directions in the basal plane. Using real-space infrared nanoimaging of the propagating phonon polaritons, we demonstrated various wavefront geometries and polariton topological transitions by twisting stacked α-MoO_3 slabs with δ from 0° to 90° (Fig. 1a). The phonon polariton twisting tunability originates from the electromagnetic hybridization between directional phonon polaritons in the top and bottom α-MoO_3 slabs and strongly depends on δ. Since a variety of polariton wavefront geometries—such as open hyperbola, 'parenthesis shaped', closed oval and squircle, as well as their deformation, including compression and stretching—can all be achieved simply by varying δ, twisted α-MoO_3 holds promise for producing tunable infrared nanolight for various nanophotonic functionalities.

The infrared nanoimaging of phonon polaritons in twisted α-MoO_3 was performed using scattering-type scanning near-field optical microscopy (s-SNOM). s-SNOM is based on a tapping-mode atomic force microscope (AFM) and simultaneously yields the topography and a nanoscale infrared image of the scanned area (Fig. 1a). In the experiment, the AFM tip is illuminated with an infrared laser at the frequency $\omega = 1/\lambda_0$ (where λ_0 is the wavelength of infrared light in free space), and the topography and backscattered near-field signal are recorded during the scan. The experimental observable near-field amplitude $S(\omega)$ and phase $\Phi(\omega)$ typically have a spatial resolution of ~10 nm, close to the radius of the AFM tip, and therefore can map nanopolaritons in real space[13,14,20]. The polaritons are typically imaged as fringes—standing-wave interference oscillations—in the s-SNOM experiments.

Figure 1b shows, at $\omega = 915\,\mathrm{cm}^{-1}$, a representative s-SNOM amplitude $S(\omega)$ image of a single α-MoO_3 slab. In the experiment, we fabricated Au disks (thickness, 100 nm; diameter, 1 μm) on top of the α-MoO_3 devices. The metallic Au disks can strongly concentrate electric fields—the lighting rod effect[21]—and launch[22,23] propagating phonon polaritons upon infrared illumination. Two types of phonon polariton fringes—the $S(\omega)$ oscillations—can be observed: X-shaped hyperbolic fringes around the Au disk and linear fringes close to the slab edge. The linear fringes originate from the interference between phonon polaritons launched by the

[1]Materials Research and Education Center, Department of Mechanical Engineering, Auburn University, Auburn, AL, USA. [2]Interdisciplinary Center for Quantum Information, State Key Laboratory of Modern Optical Instrumentation, ZJU-Hangzhou Global Science and Technology Innovation Center, Zhejiang University, Hangzhou, China. [3]Department of Physics, Massachusetts Institute of Technology, Cambridge, MA, USA. [4]These authors contributed equally: Mingyuan Chen, Xiao Lin. ✉e-mail: sdai@auburn.edu

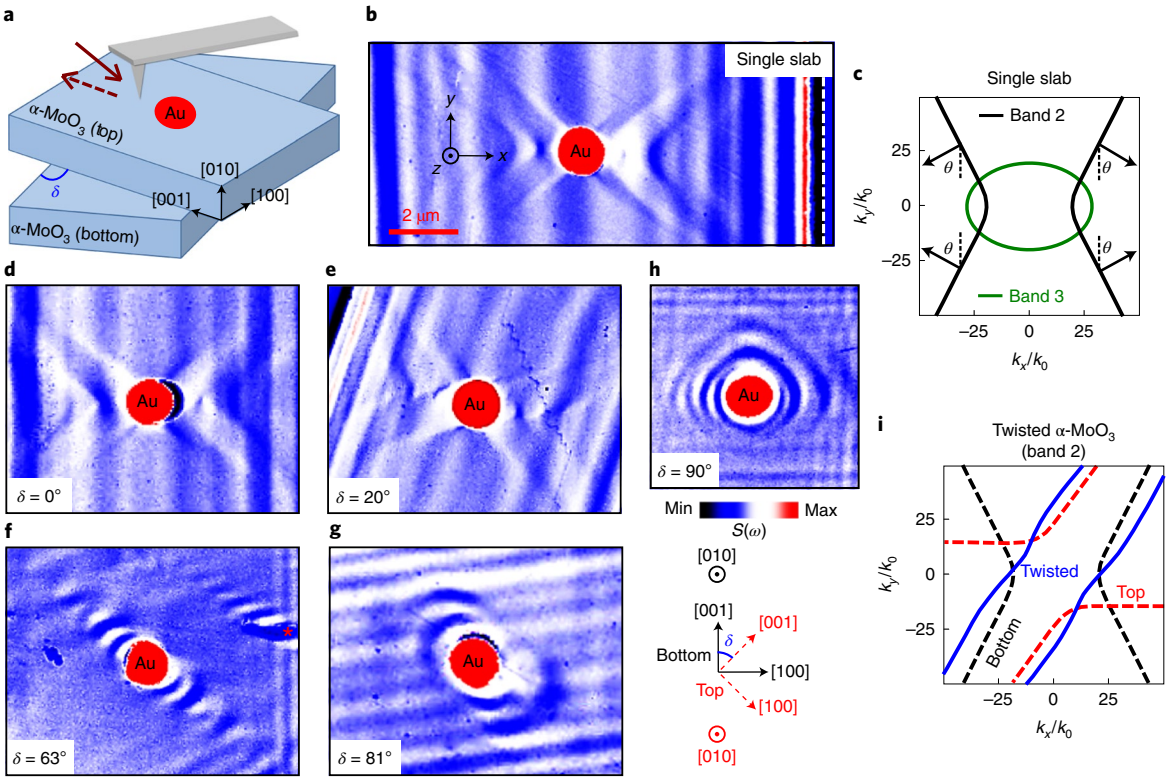

Fig. 1 | Real-space infrared nanoimages reveal the twisting tunability for phonon polaritons. a, Experiment schematic. The solid and dashed brown arrows denote the incident and backscattered infrared light at the AFM tip (grey), respectively. The light blue boxes denote the stacked α-MoO_3 slabs with crystallographic directions and δ indicated. **b**, s-SNOM amplitude image of a single slab of α-MoO_3. The white dashed line indicates the edge of the sample. **c**, Isofrequency curves of phonon polaritons in reststrahlen bands 2 and 3. The black arrows indicate the direction of phonon polariton momentum with angle θ to the vertical (y) direction. **d**–**h**, s-SNOM amplitude images of twisted α-MoO_3 with $\delta = 0°$ (**d**), 20° (**e**), 63° (**f**), 81° (**g**) and 90° (**h**). The red asterisk in **f** marks phonon polariton fringes launched by a defect. [100], [001] and [010] in **h** denote crystallographic directions of the bottom (black) and top (red) α-MoO_3. Infrared frequencies: 915 cm^{-1} (**b**), 915 cm^{-1} (**d**), 910 cm^{-1} (**e**), 920 cm^{-1} (**f**), 915 cm^{-1} (**g**), 905 cm^{-1} (**h**). **i**, Isofrequency curves of twisted α-MoO_3 (blue solid curve), the top α-MoO_3 slab (red dashed curve) and the bottom α-MoO_3 slab (black dashed curve). Note that while ω varies slightly from 905 to 920 cm^{-1} for better visibility of polariton fringes in this figure, the same twisting configuration and topological transitions of polaritons have also been observed at the fixed frequencies $\omega = 910$ cm^{-1} (Supplementary Fig. 1) and $\omega = 915$ cm^{-1} (Supplementary Fig. 2).

s-SNOM tip and those reflected at the crystal edges. These fringes are always parallel to the crystal edge[22,23] regardless of the polariton wavefront geometry. The X-shaped fringes around the Au disk are interference patterns between phonon polaritons launched by the Au disk and the incident infrared illumination (Fig. 1a)[22,23]. For highly confined polaritons in vdW materials[22,24], these fringes superposition with the wavefront of the launched polaritons and are the main subject of this work. In contrast to spreading concentric fringes from other vdW materials, the X-shaped fringes observed in α-MoO_3 indicate the extreme anisotropy of the phonon polaritons, which propagate only along certain directions. This propagation directionality stems from the hyperbolic response ($\varepsilon_i\varepsilon_j < 0$, where ε_i and ε_j are the permittivity along different directions, and i and j denote the crystal axes [100], [001] or [010]) inside the reststrahlen bands of α-MoO_3 (refs. [18,19]): band 1 at $\omega = 542$–856 cm^{-1} for [001] phonons ($\varepsilon_{[100]} > 0$, $\varepsilon_{[001]} < 0$ and $\varepsilon_{[010]} > 0$); band 2 at $\omega = 816$–976 cm^{-1} for [100] phonons ($\varepsilon_{[100]} < 0$, $\varepsilon_{[001]} > 0$ and $\varepsilon_{[010]} > 0$); and band 3 at $\omega = 956$–$1{,}012$ cm^{-1} for [010] phonons ($\varepsilon_{[100]} > 0$, $\varepsilon_{[010]} > 0$ and $\varepsilon_{[010]} < 0$). Specifically, the directional X-shaped fringes (Fig. 1b) are directly attributed to the basal plane hyperbolic response ($\varepsilon_{[100]}\varepsilon_{[001]} < 0$) inside reststrahlen band 2: the isofrequency dispersion for the α-MoO_3 slab is an open hyperbola (Fig. 1c, black curve) in the basal plane, and phonon polaritons propagate along fixed directions (Fig. 1c, black arrows), with an angle $\theta = \arctan\sqrt{|\varepsilon_{[100]}/\varepsilon_{[010]}|}$ to the [010] direction[25–27].

The existence of directional phonon polaritons in the basal plane suggests that twisting stacked α-MoO_3 slabs inside reststrahlen band 2 offers the tunability. The advance of the stacked slabs over the single slab is revealed in the variety of shapes and topologies of the polariton isofrequency curve, which can be tuned by twisting (Fig. 1i), while the isofrequency curve in a single slab is fundamentally rigid. Fig. 1d–h shows s-SNOM images of phonon polaritons in twisted α-MoO_3 at various δ. The s-SNOM images are oriented with all the [001] axes of the bottom α-MoO_3 slab aligned vertically (see the coordinate axis in Fig. 1). At $\delta = 0°$, the phonon polaritons exhibit X-shaped fringes (Fig. 1d) that correspond to the hyperbolic wavefront, very similar to that of the single slab of α-MoO_3 (Fig. 1b). At $\delta = 20°$ (Fig. 1e), the hyperbolic wavefront can still be observed but is tilted from that at $\delta = 0°$ and the single slab. The phonon polariton wavefront at $\delta = 63°$ is different: the fringes can only be observed along a tilted line across the Au disk (Fig. 1f), the wavefront geometry is a parenthesis shaped and propagation along other directions is prohibited. This parenthesis-shaped wavefront is also revealed in phonon polariton fringes launched by a defect (Fig. 1f), where similar parenthesis-shaped fringes along the same direction can be observed. At $\delta = 81°$ (Fig. 1g), the phonon polariton wavefront becomes oval, appearing as fringes observed around the Au disk. Finally, at $\delta = 90°$ (Fig. 1h), the wavefront appears as a squircle; rounded square phonon polariton fringes are observed. In Fig. 1h,

the squircle fringes are less visible on the lower left side of the Au disk, due to the shadowing effect of the AFM cantilever[22].

The s-SNOM images in Fig. 1 reveal various wavefront geometries and topological transitions of the phonon polaritons in twisted α-MoO_3. As δ increases from 0° to 90°, the phonon polariton wavefront successively exhibits a range of shapes: hyperbola (Fig. 1d, $\delta=0°$), tilted hyperbola (Fig. 1e, $\delta=20°$), parenthesis (Fig. 1f, $\delta=63°$), oval (Fig. 1g, $\delta=81°$) and squircle (Fig. 1h, $\delta=90°$). Note that at $\delta\approx63°$, the phonon polariton wavefront changes from an open, hyperbola-like geometry (Fig. 1d,e) to closed, ellipsoidal geometries (Fig. 1g,h), corresponding to the topological transitions[26,27]. This continuous twisting tunability of phonon polaritons in α-MoO_3 over the broad range $\delta=0°$ to 90° is in stark contrast to that in twisted graphene and graphene/hexagonal boron nitride heterostructures where plasmon polaritons are affected by the moiré superlattice[15–17] at specific and small twisting angles ($\delta<5°$).

The observed twisting-derived tunability of these phonon polaritons is supported by both finite-element method (FEM) simulation and electromagnetic wave theory (Fig. 2). With the input of α-MoO_3 slab thickness and ω from our experiment and fitted α-MoO_3 permittivity based on refs. [19,28], we simulate the real-space electromagnetic field E_z and modelled momentum space (k-space) isofrequency dispersion in twisted α-MoO_3. In the real-space simulation (Supplementary Information 4), a vertical dipole (centres of Fig. 2a–f, top) was placed above the twisted α-MoO_3 as the polariton launcher. The real-space simulation reproduces the topological transitions of phonon polaritons in our experiment (Fig. 1): the wavefront exhibits a hyperbola at the single slab and $\delta=0°$ (Fig. 2a,b, top), a tilted hyperbola at $\delta=20°$ (Fig. 2c, top), a parenthesis at $\delta=63°$ (Fig. 2d, top), an oval at $\delta=81°$ (Fig. 2e, top) and a squircle at $\delta=90°$ (Fig. 2f, top). Our electromagnetic theory (Supplementary Information 5) of the isofrequency dispersion in twisted α-MoO_3 was developed from previous work on black phosphorus[29,30] and graphene metasurfaces[26,31]. The modelled k-space isofrequency curves (Fig. 2a–f, bottom) are in excellent agreement with the real-space images produced in our experiment (Fig. 1) and FEM simulations (Fig. 2a–f, top).

We attribute the twisting tunability reported in Figs. 1 and 2 to electromagnetic interactions between directional phonon polaritons in the stacked top and bottom α-MoO_3 slabs. Specifically, twisting tunability in α-MoO_3 requires extreme basal-plane anisotropy and sufficient out-of-plane field span for phonon polaritons. In Fig. 3, we provide experimental data and calculation analysis to demonstrate these criteria. At a representative infrared frequency $\omega=980\,cm^{-1}$ in reststrahlen band 3, the k-space isofrequency curve is an ellipse (Fig. 1c) and phonon polaritons propagate with an elliptical wavefront in real space (Fig. 3a). Compared with directional phonon polaritons in band 2 (Fig. 1b), phonon polaritons at $\omega=980\,cm^{-1}$ lack sufficient anisotropy and hence spread in all directions (Fig. 3a). The twisting tunability is ineffective at $\omega=980\,cm^{-1}$: phonon polaritons in twisted α-MoO_3 with $\delta=20°$ (Fig. 3b), 63° (Fig. 3c) and 90° (Fig. 3d) all exhibit an elliptical wavefront, similar to that in the single slab (Fig. 3a). These results are in stark contrast with the s-SNOM image at $\omega=900\,cm^{-1}$ (Fig. 3f) where the squircle and a series of other wavefronts (Fig. 1) can be tuned by twisting the α-MoO_3 slabs.

In addition to the extreme anisotropy in the basal plane, a sufficient out-of-plane field span is also required to create adequate electromagnetic hybridization in twisted α-MoO_3 to tune phonon polaritons. Since phonon polaritons exponentially decay outside of the α-MoO_3 slab, this criterion corresponds to a moderate decay of the phonon polariton field. Figure 3g shows the calculated distribution of electromagnetic field $|\mathbf{E}_z|$ away from the α-MoO_3 slab at three representative infrared frequencies: $\omega=900$ and $935\,cm^{-1}$ in band 2 and $\omega=980\,cm^{-1}$ in band 3. Away from the α-MoO_3 slab, the polariton field $|\mathbf{E}_z|$ decays quickly at $\omega=935$ and $980\,cm^{-1}$ but moderately

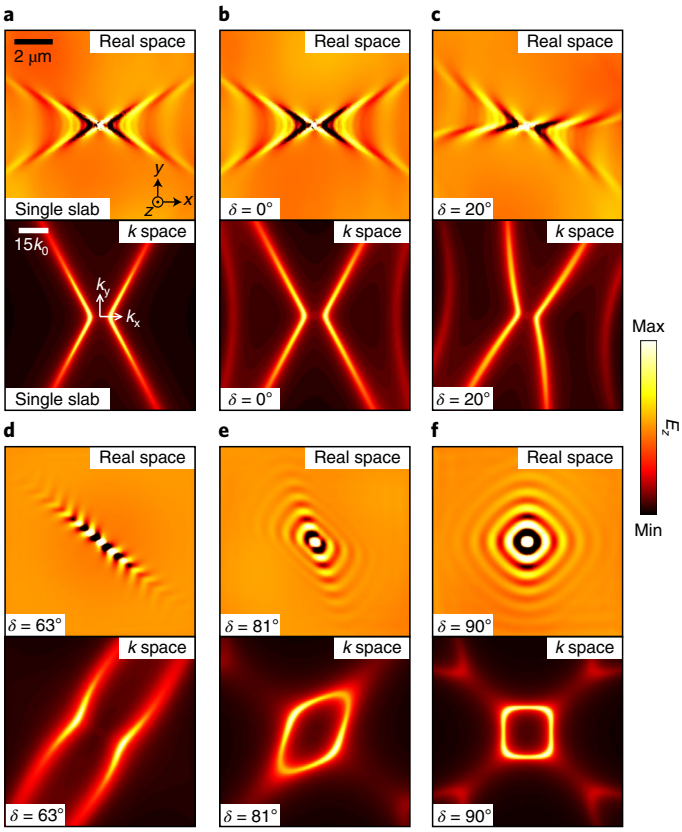

Fig. 2 | FEM real-space simulation and electromagnetic theory of momentum-space (k-space) isofrequency dispersion of phonon polaritons in twisted α-MoO_3. a–f, Top: real-space FEM simulation of phonon polaritons in a single slab of α-MoO_3 (**a**) and twisted α-MoO_3 (**b**–**f**) where a dipole was placed above the centre of the image to launch the phonon polaritons. Bottom: electromagnetic theory of corresponding isofrequency curves for a single slab of α-MoO_3 (**a**) and twisted α-MoO_3 (**b**–**f**). k_0 is the momentum of infrared photon $k_0=2\pi/\lambda_0$. Twisting angles: $\delta=0°$ (**b**), $\delta=20°$ (**c**), $\delta=63°$ (**d**), $\delta=81°$ (**e**), $\delta=90°$ (**f**).

at $\omega=900\,cm^{-1}$: the field decay length where $|\mathbf{E}_z|$ becomes $1/e$ of that at $z=0$ is 14, 92 and 243 nm for $\omega=980$, 935 and $900\,cm^{-1}$, respectively. Therefore, in the out-of-plane direction, the α-MoO_3 phonon polariton field spans sufficiently at $\omega=900\,cm^{-1}$ but insufficiently at $\omega=935$ and $980\,cm^{-1}$. In vertically stacked α-MoO_3 devices, sufficient field span of phonon polaritons from each α-MoO_3 slab leads to adequate electromagnetic interaction and thus to twisting tunability at $\omega=900\,cm^{-1}$. Our s-SNOM data in Fig. 3d–f support this theoretical assertion. Evident twisting tunability was observed at $\omega=900\,cm^{-1}$ (Figs. 1 and 3f) while a lack of twisting configuration was observed at $\omega=935$ and $980\,cm^{-1}$. Note that at $\omega=935\,cm^{-1}$ (Fig. 3e), the phonon polaritons in the top and bottom α-MoO_3 slab fulfil the other criterion to be anisotropic in the basal plane (hyperbolic wavefront), yet these hyperbolic modes barely interact with each other due to their insufficient out-of-plane field span (Fig. 3g). Similar results were observed in α-MoO_3 slabs with another twisting angle at the same frequency (Supplementary Fig. 3).

We emphasize that while the methodology for tuning phonon polaritons in twisted α-MoO_3 is similar to that for twistronics[2] in moiré engineering, their physical origins are different. The former stems from angle-dependent electromagnetic hybridization between anisotropic phonon polariton fields in stacked α-MoO_3, whereas the latter is attributed to the peculiar electronic band structure modified by vdW superlattices. Therefore, phonon polaritons

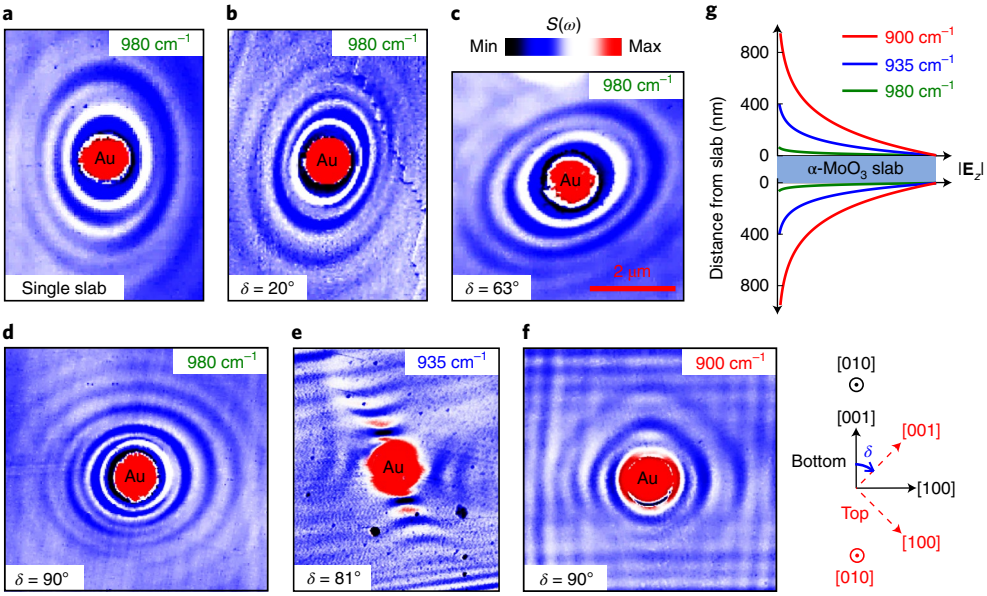

Fig. 3 | Electromagnetic interaction as the origin of twisting tunability for phonon polaritons. a–d, s-SNOM amplitude images of a single slab of α-MoO_3 (**a**) and twisted α-MoO_3 with $\delta = 20°$ (**b**), 63° (**c**) and 90° (**d**) at $\omega = 980\ cm^{-1}$. **e**, s-SNOM amplitude images of twisted α-MoO_3 with $\delta = 81°$ at $\omega = 935\ cm^{-1}$. **f**, s-SNOM amplitude images of twisted α-MoO_3 with $\delta = 90°$ at $\omega = 900\ cm^{-1}$. [100], [001] and [010] in **f** denote crystallographic directions of the bottom (black) and top (red) α-MoO_3. **g**, Theoretical electromagnetic field distribution $|\mathbf{E}_z|$ (horizontal axis) along the [100] direction away from the α-MoO_3 slab at $\omega = 900$, 935 and 980 cm^{-1}. α-MoO_3 thickness, 100 nm.

in twisted α-MoO_3 can be tuned via twisting in a broad range of angle δ from 0° to 90° and are relatively less sensitive to δ, whereas twistronics is mainly investigated in vdW heterostructures at small twisting angles (typically $\delta < 5°$) and is highly sensitive to δ. Note that the electromagnetic interaction nature of the twisting tunability of phonon polaritons was further confirmed by dispersion analysis of phonon polaritons (Supplementary Section 7).

The combined experimental and theoretical results in Figs. 1–3 show the tuning of phonon polaritons in twisted α-MoO_3. The phonon polariton wavefront can be altered by controlling δ between stacked α-MoO_3 slabs in a broad range of 0°–90°, thus demonstrating the extended vdW configurability of nanoscale electromagnetic energy beyond moiré engineering at small twisting angles[2–7]. The observed twisting tunability of polaritons is attributed to the electromagnetic interaction between anisotropic polariton fields and is highly dependent on the twisting angle. Note that by altering the wavefront via twisting, the tuning of phonon polariton propagation direction and wavelength surpasses previous modulation efforts through refractive index engineering[32,33] or vdW heterostructuring[34,35]. Future work may be guided towards exploring the dynamics and reconfigurability of twisted polariton nanolight via nanomechanical manipulation[2] or vdW photonic hybrids[1,35–37]. The phonon polariton wavefronts and topologies demonstrated in this work suggest the opportunity to produce polariton nanolight with tailored propagating properties and photonic density of states[38,39] for on-demand nanophotonic functionalities that can benefit light emission[39], super-Planckian thermal emission[40], quantum optics[41,42], exotic transitions[43], and so on. In addition, the directional phonon polaritons, especially their collimated and diffractionless propagation at the topological transition angle ($\delta \approx 63°$, Fig. 3f) can be further explored for exotic nano-optical phenomena, including super-Coulombic long-range dipolar interactions[44]. Finally, the twisting tunability of phonon polaritons in α-MoO_3 also provides a prototype for the exploration of configuring other anisotropic physical properties in vdW materials via twisting, stacking and heterostructuring.

It should be noted that after the submission of our paper, we became aware of three other manuscripts reporting the observation of tunable phonon polaritons in twisted α-MoO_3 bilayers[45–47].

Online content

Any methods, additional references, Nature Research reporting summaries, source data, extended data, supplementary information, acknowledgements, peer review information; details of author contributions and competing interests; and statements of data and code availability are available at https://doi.org/10.1038/s41563-020-0732-6.

Received: 24 April 2020; Accepted: 12 June 2020;
Published online: 13 July 2020

References

1. Novoselov, K. S., Mishchenko, A., Carvalho, A. & Castro Neto, A. H. 2D materials and van der Waals heterostructures. *Science* **353**, aac9439 (2016).
2. Ribeiro-Palau, R. et al. Twistable electronics with dynamically rotatable heterostructures. *Science* **361**, 690–693 (2018).
3. Ponomarenko, L. A. et al. Cloning of Dirac fermions in graphene superlattices. *Nature* **497**, 594–597 (2013).
4. Dean, C. R. et al. Hofstadter's butterfly and the fractal quantum Hall effect in moiré superlattices. *Nature* **497**, 598–602 (2013).
5. Hunt, B. et al. Massive Dirac fermions and Hofstadter butterfly in a van der Waals heterostructure. *Science* **340**, 1427–1430 (2013).
6. Cao, Y. et al. Unconventional superconductivity in magic-angle graphene superlattices. *Nature* **556**, 43–50 (2018).
7. Sharpe, A. L. et al. Emergent ferromagnetism near three-quarters filling in twisted bilayer graphene. *Science* **365**, 605–608 (2019).
8. Tran, K. et al. Evidence for moiré excitons in van der Waals heterostructures. *Nature* **567**, 71–75 (2019).
9. Alexeev, E. M. et al. Resonantly hybridized excitons in moiré superlattices in van der Waals heterostructures. *Nature* **567**, 81–86 (2019).
10. Jin, C. et al. Observation of moiré excitons in WSe_2/WS_2 heterostructure superlattices. *Nature* **567**, 76–80 (2019).
11. Seyler, K. L. et al. Signatures of moiré-trapped valley excitons in $MoSe_2/WSe_2$ heterobilayers. *Nature* **567**, 66–70 (2019).
12. Basov, D. N., Fogler, M. M. & García de Abajo, F. J. Polaritons in van der Waals materials. *Science* **354**, aag1992 (2016).

13. Low, T. et al. Polaritons in layered two-dimensional materials. *Nat. Mater.* **16**, 182–194 (2016).
14. Ni, G. X. et al. Plasmons in graphene moiré superlattices. *Nat. Mater.* **14**, 1217–1222 (2015).
15. Sunku, S. S. et al. Photonic crystals for nano-light in moire graphene superlattices. *Science* **362**, 1153–1156 (2018).
16. Jiang, L. et al. Soliton-dependent plasmon reflection at bilayer graphene domain walls. *Nat. Mater.* **15**, 840–844 (2016).
17. Hu, F. et al. Real-space imaging of the tailored plasmons in twisted bilayer graphene. *Phys. Rev. Lett.* **119**, 247402 (2017).
18. Ma, W. et al. In-plane anisotropic and ultra-low-loss polaritons in a natural van der Waals crystal. *Nature* **562**, 557–562 (2018).
19. Zheng, Z. et al. A mid-infrared biaxial hyperbolic van der Waals crystal. *Sci. Adv.* **5**, eaav8690 (2019).
20. Dai, S. et al. Tunable phonon polaritons in atomically thin van der Waals crystals of boron nitride. *Science* **343**, 1125–1129 (2014).
21. Atkin, J. M., Berweger, S., Jones, A. C. & Raschke, M. B. Nano-optical imaging and spectroscopy of order, phases, and domains in complex solids. *Adv. Phys.* **61**, 745–842 (2012).
22. Dai, S. et al. Efficiency of launching highly confined polaritons by infrared light incident on a hyperbolic material. *Nano Lett.* **17**, 5285–5290 (2017).
23. Alonso-González, P. et al. Controlling graphene plasmons with resonant metal antennas and spatial conductivity patterns. *Science* **344**, 1369–1373 (2014).
24. Hu, G., Shen, J., Qiu, C.-W., Alù, A. & Dai, S. Phonon polaritons and hyperbolic response in van der Waals materials. *Adv. Opt. Mater.* **8**, 1901393 (2020).
25. Caldwell, J. D. et al. Sub-diffractional volume-confined polaritons in the natural hyperbolic material hexagonal boron nitride. *Nat. Commun.* **5**, 5221 (2014).
26. Gomez-Diaz, J. S., Tymchenko, M. & Alù, A. Hyperbolic plasmons and topological transitions over uniaxial metasurfaces. *Phys. Rev. Lett.* **114**, 233901 (2015).
27. Krishnamoorthy, H. N., Jacob, Z., Narimanov, E., Kretzschmar, I. & Menon, V. M. Topological transitions in metamaterials. *Science* **336**, 205–209 (2012).
28. Álvarez-Pérez, G. et al. Infrared permittivity of the biaxial van der Waals semiconductor α-MoO_3 from near- and far-field correlative studies. *Adv. Mater.* https://doi.org/10.1002/adma.201908176 (2020).
29. Renuka, M. et al. Dispersion engineering of hyperbolic plasmons in bilayer 2D materials. *Opt. Lett.* **43**, 5737–5740 (2018).
30. Nemilentsau, A., Low, T. & Hanson, G. Anisotropic 2D materials for tunable hyperbolic plasmonics. *Phys. Rev. Lett.* **116**, 066804 (2016).
31. Hu, G., Krasnok, A., Mazor, Y., Qiu, C.-W. & Alù, A. Moiré hyperbolic metasurfaces. *Nano Lett.* **20**, 3217–3224 (2020).
32. Chaudhary, K. et al. Engineering phonon polaritons in van der Waals heterostructures to enhance in-plane optical anisotropy. *Sci. Adv.* **5**, eaau7171 (2019).
33. Fali, A. et al. Refractive index-based control of hyperbolic phonon-polariton propagation. *Nano Lett.* **19**, 7725–7734 (2019).
34. Brar, V. W. et al. Hybrid surface-phonon-plasmon polariton modes in graphene/monolayer h-BN heterostructures. *Nano Lett.* **14**, 3876–3880 (2014).
35. Dai, S. et al. Graphene on hexagonal boron nitride as a tunable hyperbolic metamaterial. *Nat. Nanotechnol.* **10**, 682–686 (2015).
36. Woessner, A. et al. Highly confined low-loss plasmons in graphene–boron nitride heterostructures. *Nat. Mater.* **14**, 421–425 (2015).
37. Caldwell, J. D. et al. Atomic-scale photonic hybrids for mid-infrared and terahertz nanophotonics. *Nat. Nanotechnol.* **11**, 9–15 (2016).
38. Jacob, Z. et al. Engineering photonic density of states using metamaterials. *Appl. Phys. B* **100**, 215–218 (2010).
39. Galfsky, T., Gu, J., Narimanov, E. E. & Menon, V. M. Photonic hypercrystals for control of light-matter interactions. *Proc. Natl Acad. Sci. USA* **114**, 5125–5129 (2017).
40. Guo, Y., Cortes, C. L., Molesky, S. & Jacob, Z. Broadband super-Planckian thermal emission from hyperbolic metamaterials. *Appl. Phys. Lett.* **101**, 131106 (2012).
41. Hoang, T. B., Akselrod, G. M. & Mikkelsen, M. H. Ultrafast room-temperature single photon emission from quantum dots coupled to plasmonic nanocavities. *Nano Lett.* **16**, 270–275 (2016).
42. Bogdanov, S. I. et al. Ultrabright room-temperature sub-nanosecond emission from single nitrogen-vacancy centers coupled to nanopatch antennas. *Nano Lett.* **18**, 4837–4844 (2018).
43. Rivera, N., Kaminer, I., Zhen, B., Joannopoulos, J. D. & Soljacic, M. Shrinking light to allow forbidden transitions on the atomic scale. *Science* **353**, 263–269 (2016).
44. Newman, W. D. et al. Observation of long-range dipole–dipole interactions in hyperbolic metamaterials. *Sci. Adv.* **4**, eaar5278 (2018).
45. Duan, J. et al. Twisted nano-optics: manipulating light at the nanoscale with twisted phonon polaritonic slabs. *Nano Lett.* https://doi.org/10.1021/acs.nanolett.0c01673 (2020).
46. Hu, G. et al. Topological polaritons and photonic magic angles in twisted α-MoO_3 bilayers. *Nature* **582**, 209–213 (2020).
47. Zheng, Z. et al. Phonon polaritons in twisted double-layers of hyperbolic van der Waals crystals. *Nano Lett.* https://doi.org/10.1021/acs.nanolett.0c01627 (2020).

Methods

Fabrication of twisted α-MoO_3 structures. α-MoO_3 slabs were mechanically exfoliated from bulk crystals. Due to the anisotropic crystal structure, the crystallographic axes can be identified according to the long straight edge of the exfoliated α-MoO_3 slab using optical microscopy and atomic force microscopy. The stacked α-MoO_3 slabs were fabricated using the dry-transfer technique[6]. Briefly, the poly(bisphenol A carbonate)/polydimethylsiloxane were used to pick up exfoliated α-MoO_3 slab, rotate manually by a specific angle according to the long straight edge and stack on another α-MoO_3 slab to form twisted α-MoO_3 structures. Electron-beam lithography and metal thermal evaporation were used to fabricate small Au disks (diameter 1 μm, thickness 100 nm) on the twisted α-MoO_3.

Infrared nanoimaging. The infrared nanoimaging of polaritons in twisted α-MoO_3 introduced in the main text was performed by s-SNOM using a commercially available microscope (neaspec). In the experiment, the AFM tip (radius ~10 nm, PtIr coating) was illuminated by monochromatic mid-infrared quantum cascade lasers (DRS Daylight Solutions) with a frequency coverage from 900 to 2,300 cm^{-1}. The s-SNOM nanoimages were recorded by a pseudoheterodyne interferometric detection module with an AFM tapping frequency of ~280 kHz and a tapping amplitude of ~70 nm. The detected signal was demodulated at the third harmonics of the tapping frequency to obtain the pure near-field output.

Data availability

All other data that support the findings of this study are available from the corresponding author upon reasonable request. Source data are provided with this paper.

Code availability

The custom code employed in this work to perform all calculations is available from the corresponding author upon reasonable request.

Acknowledgements

We acknowledge helpful discussions with X. Jiang, J. Lin and T. Low. Work at Auburn University was supported by the Auburn University Intramural Grants Program and National Science Foundation under grant no. DMR-2005194. Work in P.J.-H.'s group was supported through AFOSR grant FA9550-16-1-0382 (fabrication), and the Gordon and Betty Moore Foundation's EPiQS Initiative through grant GBMF4541 to P.J.-H. This work made use of the Materials Research Science and Engineering Center Shared Experimental Facilities supported by the National Science Foundation (NSF) (grant number DMR-0819762). The work at Zhejiang University was sponsored by the National Natural Science Foundation of China (NNSFC) under grant numbers 61625502, 11961141010 and 61975176, the Top-Notch Young Talents Program of China, and the Fundamental Research Funds for the Central Universities.

Author contributions

M.C. and X.L. contributed equally to this work. S.D. conceived the idea and designed the experiments. M.C. performed the optical experiments. T.D., Z.Z. and Q.M. prepared the samples. X.L. and H.C. developed the theory. M.C. and J.S. performed the simulation. M.C. and S.D. analysed the data. M.C., S.D. and X.L. wrote the manuscript, with input and comments from all authors. S.D., H.C. and P.J.-H. supervised the project.

Competing interests

The authors declare no competing interests.

Additional information

Supplementary information is available for this paper at https://doi.org/10.1038/s41563-020-0732-6.

Correspondence and requests for materials should be addressed to S.D.

Reprints and permissions information is available at www.nature.com/reprints.